Monthly Notices
of the
ROYAL ASTRONOMICAL SOCIETY

MNRAS **457,** 1507–1521 (2016) doi:10.1093/mnras/stw052

The BepiColombo MORE gravimetry and rotation experiments with the ORBIT14 software

S. Cicalò,[1⋆] G. Schettino,[2⋆] S. Di Ruzza,[1] E. M. Alessi,[3] G. Tommei[2⋆] and A. Milani[2]

[1]*Space Dynamics Services s.r.l., Via Mario Giuntini 63, I-56023 Cascina (PI), Italy*
[2]*Università di Pisa, Dipartimento di Matematica, Largo B. Pontecorvo 5, I-56127 Pisa, Italy*
[3]*IFAC-CNR, Via Madonna del Piano 10, I-50019 Sesto Fiorentino (FI), Italy*

Accepted 2016 January 6. Received 2016 January 6; in original form 2015 November 17

ABSTRACT

The BepiColombo mission to Mercury is an ESA/JAXA cornerstone mission, consisting of two spacecraft in orbit around Mercury addressing several scientific issues. One spacecraft is the Mercury Planetary Orbiter, with full instrumentation to perform radio science experiments. Very precise radio tracking from Earth, on-board accelerometer and optical measurements will provide large data sets. From these it will be possible to study the global gravity field of Mercury and its tidal variations, its rotation state and the orbit of its centre of mass. With the gravity field and rotation state, it is possible to constrain the internal structure of the planet. With the orbit of Mercury, it is possible to constrain relativistic theories of gravitation. In order to assess that all the scientific goals are achievable with the required level of accuracy, full cycle numerical simulations of the radio science experiment have been performed. Simulated tracking, accelerometer and optical camera data have been generated, and a long list of variables including the spacecraft initial conditions, the accelerometer calibrations and the gravity field coefficients have been determined by a least-squares fit. The simulation results are encouraging: the experiments are feasible at the required level of accuracy provided that some critical terms in the accelerometer error are moderated. We will show that BepiColombo will be able to provide at least an order of magnitude improvement in the knowledge of Love number k_2, libration amplitudes and obliquity, along with a gravity field determination up to degree 25 with a signal-to-noise ratio of 10.

Key words: methods: numerical – space vehicles: instruments – planets and satellites: individual: Mercury.

1 INTRODUCTION

BepiColombo is an ESA-JAXA mission for the exploration of the planet Mercury, scheduled for launch in 2017 and for orbit insertion around Mercury in 2024. It includes a Mercury Planetary Orbiter (MPO) equipped with a full complement of instruments to perform radio science experiments (Benkhoff et al. 2010). The Mercury Orbiter Radio science Experiment (MORE) is one of the on-board experiments, devised for improving our understanding of both planetary geophysics and fundamental physics. MORE includes three different but linked experiments: the gravimetry and rotation experiments (Milani et al. 2001; Sánchez, Belló & Jehn 2006; Cicalò & Milani 2012) and the relativity experiment (Milani et al. 2002, 2010; Schettino et al. 2015). The main goals of these experiments are to measure the gravity field and rotation state of Mercury, constraining the size and physical state of the core and the planet internal structure (to this aim, the tracking observations will be supported by optical observations with a high-resolution on-board camera, SIMBIO-SYS Marra et al. 2005; Flamini et al. 2010) and to determine the orbit of the centre of mass of the planet allowing for precise tests of General Relativity.

In Milani et al. (2001, 2002), a detailed analysis on the gravimetry-rotation experiment and on the relativity experiment, respectively, is given. In those works, the two experiments were performed independently and the studies were part of the preliminary phase of the BepiColombo mission design. Due to the high level of complexity and to the unprecedented accuracy of MORE with respect to any other radio science experiment ever done, the development of a new software was mandatory. Thus, five years later, in 2007, the Department of Mathematics of the University of Pisa got an Italian Space Agency commission for the development of a new dedicated software for the MORE experiment. This commission is going to be terminated in 2015 and the software, called ORBIT14, is now ready for use. The ORBIT14 software is able

⋆ E-mail: cicalo@spacedys.com (SC); gschettino@mail.dm.unipi.it (GS); tommei@dm.unipi.it (GT)

to generate simulated tracking observables (range and range-rate), on-board accelerometer measurements, on-board camera angular observations and to solve-for a large list of parameters of interest by a global least-squares fit. An innovative constrained multi-arc strategy is applied in the tracking measurements processing (see Alessi et al. 2012b; Cicalò & Milani 2012), and state-of-the-art error models are taken into account for each type of measurements involved. Particular care needs to be taken in considering these error models, since, for instance, the accelerometer error could spoil significantly the determination of the Mercury gravity field if not calibrated properly.

In principle, the structure of the program allows the three experiments of gravimetry, rotation and relativity to be performed at once. In this work, we describe only the main results for the gravimetry and rotation experiments of MORE, while in a future paper we will add also the relativity experiment for a comprehensive solution. All the results are obtained from a full cycle numerical simulation, including the generation of simulated measurements, and the determination, by a least-squares fit, of a long list of variables including the initial conditions for each observed arc, the calibration parameters, the gravity field harmonic coefficients and the rotation parameters. The results show the fundamental improvements that this space mission can provide and the accuracies that can be achieved, both in terms of formal covariance and systematic errors.

Recently, the NASA MESSENGER (MErcury Surface, Space ENvironment, GEochemistry and Ranging) space probe (Solomon et al. 2007), in orbit around Mercury from 2011 March until 2015 April, has greatly improved the knowledge on gravimetry and rotation state of Mercury. Nevertheless, as it will turn out to be also from the results of our simulations, BepiColombo will provide further significant improvements, mainly because of its polar orbit (400 × 1500 km, with a period of about 2.3 h) which will allow for a global coverage of the planet (Benkhoff et al. 2010); MESSENGER performed only a partial high-resolution coverage of the Northern hemisphere (Mazarico et al. 2014). Concerning in particular the radio science experiment, the MORE experiment will perform tracking observations with an unprecedented level of accuracy; moreover, the presence of an on-board accelerometer will overcome the significant problem of modelling the non-gravitational accelerations acting on the probe.

The paper is organized as follows: in Sections 2, 3 and 4 we give a general description of the tracking measurements, on-board accelerometer measurements and on-board camera measurements, including a discussion on the corresponding error models. We present the Mercurycentric dynamical model in Section 5, while in Sections 6 and 7 we describe the general settings and assumptions for the numerical tests to be performed. Finally, we show and discuss all the results in Section 8 and we draw the conclusions in Section 9. In summary, we show in Fig. 1 a scheme that better clarifies how the contents of the various sections contribute to the whole experiment.

2 RADIO TRACKING OBSERVATION MODEL

In the case of a satellite orbiting around another planet, such as in the MORE experiment, the observational technique is complicated by many factors, but it can be simply considered as a tracking from an Earth-based station, giving range and range-rate information (see Iess & Boscagli 2001).

A sketch of the dynamics used to compute the observables is showed in Fig. 2. To compute the range distance from the ground station on the Earth to the spacecraft (s/c) around Mercury, and the corresponding range-rate, we need the following state vectors, each

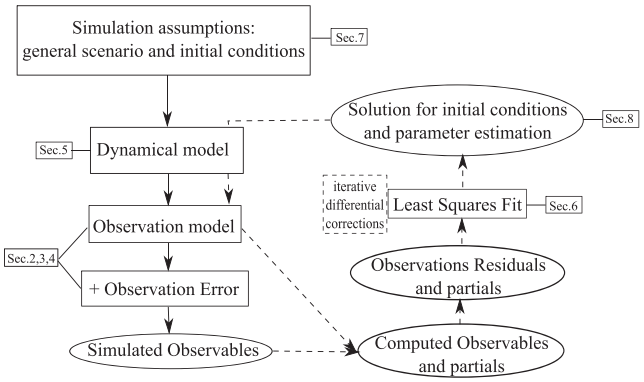

Figure 1. Scheme summarizing how the various sections contribute to the whole experiment.

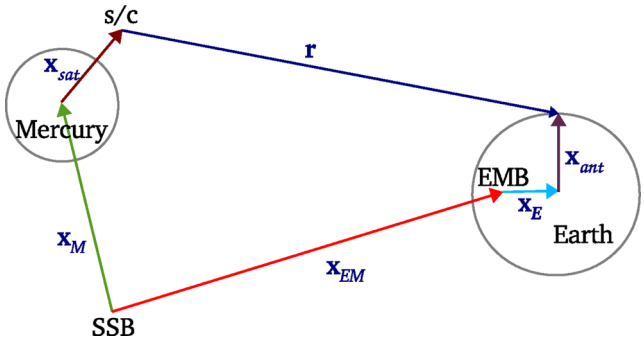

Figure 2. Multiple dynamics for the tracking of the s/c around Mercury from the Earth: $\boldsymbol{x}_{\rm sat}$ is the Mercurycentric position of the s/c, $\boldsymbol{x}_{\rm M}$ and $\boldsymbol{x}_{\rm EM}$ are the SSB positions of Mercury and of the EMB, $\boldsymbol{x}_{\rm ant}$ is the geocentric position of the ground antenna and $\boldsymbol{x}_{\rm E}$ is the position of the Earth barycenter with respect to the EMB.

one evolving according to a specific dynamical model:

(i) the Mercurycentric position of the s/c $\boldsymbol{x}_{\rm sat}$;
(ii) the Solar system barycentric (SSB) positions of Mercury and of the Earth–Moon barycenter (EMB) $\boldsymbol{x}_{\rm M}$ and $\boldsymbol{x}_{\rm EM}$;
(iii) the geocentric position of the ground antenna $\boldsymbol{x}_{\rm ant}$;
(iv) the position of the Earth barycenter with respect to the EMB $\boldsymbol{x}_{\rm E}$.

For a discussion on the corresponding dynamical and observation models see Milani et al. (2010) and Tommei, Milani & Vokrouhlicky (2010), except for the Mercurycentric dynamics of the s/c, which will be described in Section 5.

2.1 Visibility conditions

Because of the mutual geometric configuration between the directions of the antenna on the Earth's surface and the antenna on the s/c, the communication between them, and thus the tracking measurements, is not always possible or too spoiled. In our numerical simulations, we assume that certain conditions must be verified to guarantee communication between the ground antenna and the s/c. Therefore, we must take into account at least the possible occultations of the s/c by Mercury, the elevation of Mercury (and the s/c) above the horizon at the observing station (we assumed a minimum elevation of 15°) and the angle between Mercury (and the s/c) and the Sun as seen from the Earth.

Due to the visibility conditions, the observations are split in arcs conventionally defined of about one day, comprehensive of

a tracking period of 15–16 h, followed by a 'dark' period without data, which can be processed by adopting a multi-arc strategy, as discussed in Section 6.2. In practice, we terminate the arc whenever there is an interruption of the range-rate observation longer than 3 h: this interval is longer than the longest possible interruption due to occultation of the s/c by Mercury.

2.2 Range and range-rate accuracies and error models

According to Iess & Boscagli (2001), a nominal white noise can be associated with the tracking measurements error. In our case, the one-way range and range-rate observables are conventionally defined as two-ways measurements divided by 2, in cm and cm s^{-1}, respectively. Thus, assuming top accuracy performances of the transponder in *Ka* band, the following Gaussian errors have to be added to simulated range and range-rate:

$\sigma_{\rm r} = 15$ cm @ 300s;

$\sigma_{\rm rr} = 1.5 \times 10^{-4}$ cm s^{-1} @ 1000 s integration time.

When *X*-band tracking is simulated, we assume one order of magnitude lower accuracies. If the simulated integration time is different from the reference value, the standard deviation must be scaled according to Gaussian statistics. In particular, if we assume an integration time of 30 s, the corresponding error is $\sigma_{\rm rr} = 8.7 \times 10^{-4}$ cm s^{-1}.

In general, a simple white noise model could not be enough for very accurate experiments. A more realistic error model can be considered in the simulation of the range and range-rate observations, justified both by the physical models and by experience, as discussed in detail by Iess & Boscagli (2001). For the range-rate observables, a systematic component of the noise model is obtained, by inverse Fourier transform, from a noise spectrum containing separate components accounting for the known physical sources of error. However, it turned out from past simulations (e.g. Milani et al. 2001; Cicalò & Milani 2012) that the gravimetry and rotation experiments of BepiColombo are not significantly affected by this systematic component of the measurement error, thus we have not included it in this work.

From a comparison of the accuracies for the range and the range-rate it turns out that $\sigma_{\rm r}/\sigma_{\rm rr} \sim 1 \times 10^5$ s, which implies that the range-rate measurements are more accurate than the range when we are observing phenomena with a period shorter than 1×10^5 s. Since the s/c orbital period, and then the periods related to the gravity field perturbations, are less than 10^4 s, the gravimetry experiment is performed mainly with the range-rate tracking data while the opposite is true in the relativity experiment context (Milani et al. 2002). As a consequence, we will be able to investigate the effects of possible systematic components in the range error model only in a future paper dedicated to the relativity experiment.

When the orbit determination of an object orbiting around another planet is performed by radial and radial velocity observations, there is an important symmetry responsible for the weakness of the orbit determination that is an approximate version of the exact symmetry found in Bonanno & Milani (2002). In our case, if the Mercurycentric orbit is rotated around an axis $\hat{\boldsymbol{\rho}}$ in the direction from the Earth to the centre of Mercury, then there would be an exact symmetry in the range and range-rate observations if $\hat{\boldsymbol{\rho}}$ were constant and Mercury spherical. Given that $\hat{\boldsymbol{\rho}}$ changes with time, the small parameter in the approximate symmetry is the displacement angle by which $\hat{\boldsymbol{\rho}}$ rotates (in an inertial reference system) during the observation arc time span. The weak directions $\hat{\boldsymbol{w}}_{\rm dp}$ and $\hat{\boldsymbol{w}}_{\rm dv}$ of the orbit determination in the three-dimensional subspaces of the s/c Mercurycentric initial position $\boldsymbol{r}_0$ and velocity $\boldsymbol{v}_0$, respectively, are given by

$$\hat{\boldsymbol{w}}_{\rm dp} = \frac{\hat{\boldsymbol{\rho}} \times \boldsymbol{r}_0}{|\hat{\boldsymbol{\rho}} \times \boldsymbol{r}_0|}, \qquad \hat{\boldsymbol{w}}_{\rm dv} = \frac{\hat{\boldsymbol{\rho}} \times \boldsymbol{v}_0}{|\hat{\boldsymbol{\rho}} \times \boldsymbol{v}_0|}. \tag{1}$$

For this reason, we discard arcs with total duration below a minimum (2 h), because the initial conditions would be too poorly determined. Different solutions can be adopted to stabilize the solution (see Milani & Gronchi 2010, Chap. 17 and Section 6.2).

3 ON-BOARD ACCELEROMETER

The proximity of Mercury to the Sun is responsible for strong non-gravitational perturbations on the spacecraft orbit, mainly due to the direct solar radiation pressure, to the indirect radiation (thermal and albedo) from the planet's surface, and the thermal re-emission effect from the spacecraft. Due to the general difficulty of modelling these effects, an accelerometer (ISA – Italian Spring Accelerometer) will be placed on-board. This instrument is capable to measure differential accelerations between a sensitive element and its rigid frame (cage) and thus to give accurate information on the non-gravitational accelerations (Iafolla & Nozzoli 2001).

A fundamental issue to consider is that, since it measures only differential accelerations, the absolute zero of the measurement scale is a priori unknown. Moreover, if there are sources of systematic errors in the accelerometer measurements then the zero of the scale will be inevitably shifted. In particular, the thermal effects are very important, because the accelerometer is sensitive to the temperature and it acts also as a thermometer (Iafolla & Nozzoli 2001). In this paper, we include an up-to-date version of the error model as provided by the ISA team. All the relevant components of the error model are described in Section 3.1. In principle, the error model is not deterministic, meaning that it is not possible to include it in the dynamical model in a closed form. However, not including it at all would certainly be source of systematic errors in the orbit determination fit and, for this reason, it must be properly calibrated (see Section 5.6).

3.1 Accelerometer error model

The error model which describes the uncertainties affecting the accelerometer readings has been provided by ISA team (private communications).[1] In short, the model consists of the following terms.

(i) *Spacecraft orbital period term or resonant term*: it is a systematic component, which accounts for several effects, roughly described by a sinusoid at spacecraft orbital period around Mercury; the amplitude ascribed to this component is a critical issue, since we found that the results depend significantly on this choice.[2] As it will be detailed in Section 8.5, we do not calibrate at all this component at this stage, but, considering that some kind of calibration will be applied when dealing with real data, we assume a residual amplitude after calibration of 1×10^{-7} cm s^{-2}.

[1] At present moment, ISA team cannot guarantee that this will be the effective error model, since the ultimate tests will be necessarily performed during the cruise phase of the s/c.

[2] Note that this component has the same period of the simulated signal.

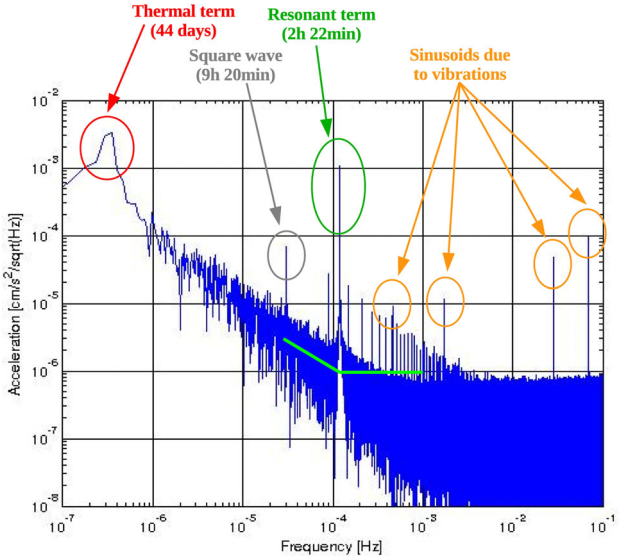

Figure 3. Spectrum of the ISA error model integrated over 88 d.

(ii) *Mercury sidereal period term or main thermal term*: it is a systematic component described by a sinusoid at Mercury orbital period around the Sun with amplitude 4.2×10^{-6} cm s^{-2}.

(iii) *Other systematic components*: they take into account thermal disturbances from adjacent units and vibrations and are described by a square wave at 3.5×10^{-5} Hz and four sinusoids at 2×10^{3}, 6×10^{2}, 36, 14 s, respectively.

(iv) *Random component*: it consists of a random background at 10^{-6} cm s$^{-2}/\sqrt{\text{Hz}}$ in the measurement bandwidth (between 3×10^{-5} Hz and 10^{-1} Hz) and a random rise at low frequencies starting from 5×10^{-4} Hz.

We remark that the random term does not fulfil the original mission requirements (document: BC-EST-RS-02256), where it was pointed out that the low-frequency random rise should have taken place below 10^{-4} Hz, while the present model implies that the random background is already a factor of 3 larger than requirements at 10^{-4} Hz. This component results somehow critical, particularly for the determination of some rotational parameters. Since the low-frequency random rise behaviour will be definitively confirmed only after the cruise phase tests, we assume to neglect its contribution to the error model in the nominal scenario, checking its effects with a further separated investigation.

Fig. 3 shows the spectrum of the error model integrated over 88 d; the superimposed thick line shows the expected behaviour from requirements for a comparison.

4 ON-BOARD CAMERA

As regards the rotation experiment, the range and range-rate tracking measurements can be combined with the optical measurements performed by the on-board High Resolution Imaging Camera (part of the on-board instrument SYMBIO-SYS), which can constrain the rotation angles by matching pairs of high-resolution images of the same portion of the surface. The rotation state of Mercury and the s/c orbit can be completely determined by tracking observables, see Cicalò & Milani (2012), hence, the basic idea is that the addition of the optical observables can improve the parameters fit. The simulations results of Section 8 will show how significant could be this improvement, in relation to the accuracy of the measurements.

4.1 Definition of angular observables

Let us consider a number of reference points on the Mercury surface, defining a geodetic network on the planet. For the purpose of the simulations, these points will be chosen randomly but uniformly distributed on the surface.[3] We consider the motion of the spacecraft orbiting around Mercury and we check if each point is seen from the spacecraft by the on-board camera. That is, we check some visibility conditions between each point and the spacecraft. When the visibility conditions are satisfied, the ecliptic latitude and the ecliptic longitude of the point with respect to the spacecraft in a satellite-centric space-fixed frame of reference are computed.

Each point $\boldsymbol{\nu}$ on the surface of Mercury can be defined by body-fixed spherical coordinates (λ, θ, r), where $\lambda \in [0, 2\pi)$ and $\theta \in (-\pi/2, \pi/2)$ are, respectively, the longitude and the latitude of the reference point and r is the distance from the centre of mass of Mercury.[4] Let $\mathbf{R}(t)$ be the rotation matrix from the Mercurycentric space-fixed ecliptic $J2000$ to the Mercurycentric body-fixed coordinates as will be defined in Section 5. Then, denoting with $\boldsymbol{\nu}_{\rm bf}$ the Cartesian coordinates of each point in the Mercurycentric body-fixed frame of reference, the space-fixed coordinates of a reference point $\boldsymbol{\nu}$ is given by $\boldsymbol{\nu}_{\rm sf} = \mathbf{R}^{\rm T}(t)\, \boldsymbol{\nu}_{\rm bf}$, where $\mathbf{R}^{\rm T}$ is the transpose of the matrix $\mathbf{R}$.

The vector $\boldsymbol{d}_{\rm sf} = \boldsymbol{\nu}_{\rm sf} - \boldsymbol{x}_{\rm sat}$, where $\boldsymbol{x}_{\rm sat}$ is the spacecraft position in the Mercurycentric space-fixed ecliptic frame of reference $J2000$, represents the relative position of the reference point $\boldsymbol{\nu}$ from the spacecraft in space-fixed coordinates and can be written, for convenience, in terms of polar coordinates (α, δ) as $\boldsymbol{d}_{\rm sf} = (\cos\delta\cos\alpha, \cos\delta\sin\alpha, \sin\delta)|\boldsymbol{d}_{\rm sf}|$, where $\alpha \in [0, 2\pi)$ and $\delta \in (-\pi/2, \pi/2)$ are, respectively, the *ecliptic longitude* and the *ecliptic latitude* of the point on the Mercury surface with respect to the spacecraft. We will call the couple (α, δ) *angular observable*.

However, we need to consider the correction due to the aberration, which is due to the relative motion between $\boldsymbol{\nu}_{\rm sf}$ and $\boldsymbol{x}_{\rm sat}$. A simple formulation can be obtained as in Montenbruck & Gill (2005, Section 6.2.2), but considering the ground station as the observed point and the satellite as the observer. The time needed to the light to travel from the surface of Mercury to the spacecraft, which is $d = |\boldsymbol{d}_{\rm sf}|$ divided by the speed of light c, implies that the position of the spacecraft in $\boldsymbol{d}_{\rm sf}$ has to be computed at time $t_{\rm obs}$, while that of the reference point at time $t_{\rm obs} - d/c$. A first-order (in d/c) correction can be used, in order to obtain the new vector position:

$$\boldsymbol{d} = \boldsymbol{d}_{\rm sf} + \frac{d}{c}\boldsymbol{v}_{\rm sat}; \tag{2}$$

a second-order correction is not necessary. Note that the aberration correction term due to the rotation of the planet is negligible: being $v_{\rm p} \simeq 302.6$ cm s^{-1} the equatorial rotation velocity of Mercury, we get as maximum misplacement:

$$\Delta x = v_{\rm p}\Delta t_{\rm max} \simeq 1.5 \text{ cm}.$$

4.2 Visibility conditions

A reference point on the Mercury surface can be seen from the on-board camera if three visibility conditions are satisfied: (1) the

[3] In the real data processing, these points would be selected based on suitable optical properties of the surface and on availability of the images.

[4] For the purpose of the rotation experiment, r is not really measured, being in a direction almost parallel to the line of sight.

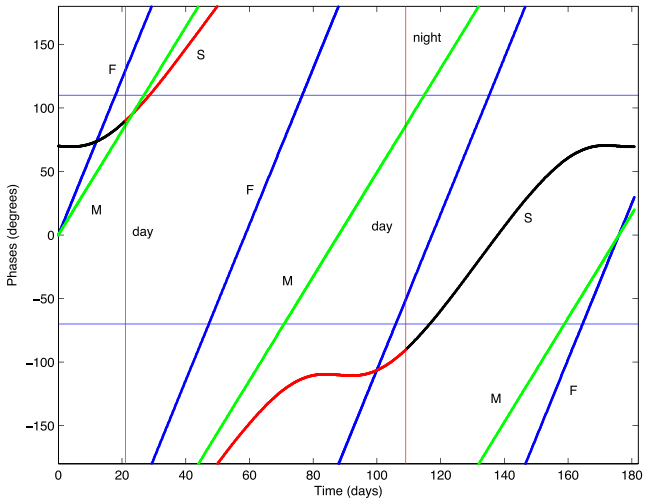

Figure 4. Visibility conditions for a point on the surface at a given longitude (represented by the two horizontal lines for ascending and descending passage) over 2 Mercury years. The lines F and M are the rotation phase and the mean anomaly of Mercury, as a function of time (in days); the curve S is the local solar time, all values in degrees. The vertical lines marked 'day' indicate the illuminated portion. Visibility occurs when one of the horizontal lines cross the S curve: there are three of these in daylight.

reference point has to be illuminated by the Sun; (2) the spacecraft is above the horizon as seen from the surface; (3) the reference point has to be in the field of view of the on-board camera (we are assuming a nadir pointing). Recalling the notation used in Section 4.1, the three conditions can be summarized in terms of scalar products as follows:

$$\boldsymbol{v}_{\rm sf} \cdot \boldsymbol{x}_{\rm sun} \geq 0; \quad \boldsymbol{v}_{\rm sf} \cdot \boldsymbol{x}_{\rm sat} \geq 0; \quad \boldsymbol{x}_{\rm sat} \cdot \boldsymbol{d}_{\rm sf} > -\beta\, |\boldsymbol{x}_{\rm sat}|\, |\boldsymbol{d}_{\rm sf}|,$$

where $\boldsymbol{x}_{\rm sun}$ is the Sun position in the Mercurycentric space-fixed ecliptic $J2000$ (such as the other vectors already defined), and $\beta > 0$ is the half aperture of the on-board camera field of view.

The configuration of the dynamical system – namely the spin-orbit resonance between Mercury and the Sun, the high eccentricity of the orbit of Mercury, the polar orbit of the MPO – creates a periodicity in the visibility of the same spot. Through this periodicity, shown in Fig. 4, we can analyse how many times the same spot can be visible from the on-board camera during the mission time.

To constrain the rotation state of the planet only observations of points seen at least twice are to be considered. Thus the points which are imaged from the spacecraft only once are discarded; the geodetic network contains only points seen more than once.[5] Moreover, if the point is seen in two consecutive passes, namely the second time is after only one revolution of the spacecraft around Mercury, we consider only one of these two observations. Indeed, the time elapsed between two consecutive revolutions is about 2.5 h, which is about $0.1\,{\rm d}/88\,{\rm d} = 1/880$ of the libration period; hence, considering two observations from consecutive orbits, the second one does not yield independent information. Due to the revolution of Mercury, a point could be seen from the spacecraft after half of the rotation period, about 28 terrestrial days, but it will be seen only if all the visibility conditions are satisfied.

[5] Points imaged just once can be added to the network, with lower accuracy.

4.3 Error budget

We assume a nadir pointing camera with a total field of view of the camera equal to 1°.47. In principle, a complete error budget shall include a star mapper error, an attitude knowledge error, thermoelastic deformations, etc. resulting in a very complex model. So, we replaced it by a very simple one, by adding a Gaussian noise of 2.5 arcsec to the angular observables. This error represents the top accuracy performances. For completeness, we simulated also the case of a 5 arcsec Gaussian error in the angular observables; the main results will be discussed in Section 8.

5 MERCURYCENTRIC DYNAMICAL MODEL

In this section, we describe the dynamical model assumed for the Mercurycentric dynamics of the MPO, i.e. for the position vector $\boldsymbol{x}_{\rm sat}$ in Fig. 2 and its velocity.

In Moyer (2000, Chap. 4), two possible approaches for the propagation of the relativistic dynamics of an Earth's satellite are described. The first one assumes the propagation of the relative motion of the satellite with respect to the Earth's centre in the SSB frame of reference, the second one assumes the propagation of the geocentric motion of the satellite in a local geocentric frame of reference, considering suitable relativistic space–time coordinates transformations. In our case, we are interested in the dynamics of a Mercury's satellite, but the principles are the same. As introduced in Section 2, we need to perform the observables computation in a common inertial SSB frame of reference, but, on the other hand, we want to propagate the motion of the spacecraft in a local Mercurycentric frame of reference, taking into account for the proper relativistic space–time coordinates conversions from the SSB frame of reference.

After the introduction of the notation used for the adopted reference frames and the transformation of coordinates, we will describe all the following terms which must be considered in the Mercurycentric acceleration of the spacecraft:

(i) Mercury gravity field spherical harmonics development (static part);
(ii) parameters for the rotation state of Mercury;
(iii) Sun, planetary and tidal perturbations;
(iv) non-gravitational perturbations and accelerometer;
(v) desaturation manoeuvers;
(vi) relativistic effects.

5.1 Relativistic frames of reference and transformations of coordinates

Let us denote by $\Psi_{\rm BC_0}$ a realization of a TDB-compatible SSB inertial frame of reference such as the Ecliptic J2000 frame of reference, where TDB is the Barycentric Dynamical Time (Soffel et al. 2003). For our purposes, this frame of reference is equivalent to the Barycentric Celestial Reference System defined in the IAU 2006 Resolution B3 (see Soffel et al. 2003; Tommei et al. 2010) up to a fixed rotation.

A second space-fixed frame of reference, which is important for the definition of the rotation state of Mercury (see Cicalò & Milani 2012), is associated with the orbit of Mercury at epoch J2000. Let us define $\Psi_{\rm BC_1} \equiv (\boldsymbol{X}_1, \boldsymbol{Y}_1, \boldsymbol{Z}_1)$, where $\boldsymbol{Z}_1$ is the orbital plane normal and $\boldsymbol{X}_1 = -\boldsymbol{X}_{\rm peri}$, with $\boldsymbol{X}_{\rm peri}$ the pericentre direction at J2000. This frame of reference can be considered TDB-compatible and let $\mathbf{R}_0$ be the fixed rotation matrix that converts the space coordinates from $\Psi_{\rm BC_0}$ to $\Psi_{\rm BC_1}$.

Now, since we want to propagate the motion of the satellite in a relativistic local Mercurycentric frame of reference, we need to define the relativistic transformations for position, velocity and time-scale from the SSB frame to the corresponding Mercurycentric frame, which we indicate with $\Psi_{\rm MC_0}$ for the space coordinates and Mercurycentric Dynamical Time TDM-compatible for the time coordinate. All these transformations are defined in Tommei et al. (2010):

$$\frac{{\rm d}T}{{\rm d}t} = 1 - \frac{U_{\rm M}}{c^2} - \frac{v_{\rm M}^2}{2c^2};$$

$$\boldsymbol{r}^{\rm BC} = \boldsymbol{r}^{\rm MC}\left(1 - \frac{U_{\rm M}}{c^2}\right) - \frac{1}{2}\left(\frac{\boldsymbol{v}_{\rm M}^{\rm BC}\cdot\boldsymbol{r}^{\rm MC}}{c^2}\right)\boldsymbol{v}_{\rm M}^{\rm BC};$$

$$\boldsymbol{v}^{\rm BC} = \left[\boldsymbol{v}^{\rm MC}\left(1 - \frac{U_{\rm M}}{c^2}\right) - \frac{1}{2}\left(\frac{\boldsymbol{v}_{\rm M}^{\rm BC}\cdot\boldsymbol{v}^{\rm MC}}{c^2}\right)\boldsymbol{v}_{\rm M}^{\rm BC}\right]\frac{{\rm d}T}{{\rm d}t}; \qquad (3)$$

where $T \equiv$ TDM, $t \equiv$ TDB, $U_{\rm M}$, $\boldsymbol{v}_{\rm M}$ are the Newtonian potential and SSB velocity of Mercury, respectively, c is the speed of light, while $\boldsymbol{r}$ and $\boldsymbol{v} = \dot{\boldsymbol{r}}$ denote the Mercurycentric position and velocity of the spacecraft, respectively. It is understood that the transformation is valid between a generic TDB-compatible SSB frame of reference and its corresponding TDM-compatible Mercurycentric frame of reference, both of them considered as space-fixed axis frames. The velocities $\boldsymbol{v}^{\rm BC}$ and $\boldsymbol{v}^{\rm MC}$ are considered with respect to TDB and TDM coordinate times, respectively.

Finally, let us introduce the Mercury body-fixed principal of inertia frame of reference $\Psi_{\rm BF}$. This frame of reference is defined in the local Mercurycentric environment, thus it is TDM-compatible. According to Cicalò & Milani (2012), under some assumptions, a semi-empirical model for the rotation of Mercury can be adopted. A rotation matrix $\mathbf{R}$ converting coordinates from the body-fixed to space-fixed $\Psi_{\rm MC_0}$ frame of reference can be easily defined as follows:

$$\boldsymbol{r}^{\rm MC_0} = \mathbf{R}^{\rm T}\boldsymbol{r}^{\rm BF},$$

where $\mathbf{R} = \mathbf{R}_3(\phi)\mathbf{R}_1(\delta_2)\mathbf{R}_2(\delta_1)\mathbf{R}_0$, $\mathbf{R}_i(\alpha)$ is the matrix associated with the rotation by an angle α about the ith axis ($i = 1, 2, 3$), (δ_1, δ_2) define the space-fixed direction of the rotation axis in the $\Psi_{\rm MC_0}$ frame and ϕ is the rotation angle around the axis, assuming the unit vector along the longest axis of the equator of Mercury (minimum momentum of inertia) as rotational reference meridian. The definition of these rotation angles will be given in Section 5.3.

5.2 Mercury gravity field spherical harmonics development (static part)

In general, a static rigid mass distributed in a region W generates outside W a potential V. With the centre of mass in the origin of the adopted frame of reference, using spherical coordinates (r, θ, λ), V can be expanded in a spherical harmonics series:

$$V(r,\theta,\lambda) = \frac{GM}{r} + \sum_{l=2}^{+\infty}\frac{GMR_{\rm M}^{\rm l}}{r^{l+1}}\sum_{m=0}^{l}P_{\rm lm}(\sin\theta)[C_{\rm lm}\cos m\lambda + S_{\rm lm}\sin m\lambda], \qquad (4)$$

where $P_{\rm lm}$ are the Legendre associated functions and M, $R_{\rm M}$ are the planet's mass and mean radius, respectively. $C_{\rm lm}$, $S_{\rm lm}$ are the potential coefficients, whose values depend on the choice of the reference system. Thus, this development is valid in a body-fixed frame of reference, such as $\Psi_{\rm BF}$, and the rotation $\mathbf{R}$ to the space-fixed Mercurycentric frame of reference $\Psi_{\rm MC_0}$ is necessary to write the equations of motion. If $\boldsymbol{a}$ is the Mercurycentric acceleration of the spacecraft due to the static gravity field at a given time, we have

$$\boldsymbol{a}^{\rm MC_0} = \mathbf{R}^{\rm T}\nabla V(\mathbf{R}\,\boldsymbol{r}^{\rm MC_0}).$$

In this way, the orbit of a satellite around the body contains information about $C_{\rm lm}$, $S_{\rm lm}$ and measuring accurately enough the orbit, it is possible to solve-for them by a least-squares fit.

5.3 Rotational dynamics

For the computation of the rotation matrix $\mathbf{R}$ we use the semi-empirical model defined in Cicalò & Milani (2012). In that paper, a detailed analysis on the Mercury rotation theory has been performed and a simplified semi-empirical rotation model has been defined for the simulations. The fundamental aspects that describe the rotation state of Mercury are the followings:

(i) the *Cassini state theory*, involving the obliquity η with respect to the orbit normal $\boldsymbol{Z}_1$, and in general the direction of the rotation axis which is expected to be coplanar with $\boldsymbol{Z}_1$ and the axis around which the orbital plane precesses because of secular planetary perturbations, averaged over long time scales, called Laplace pole (see Yseeboodt & Margot 2006);

(ii) the *librations in longitude*, including the 88 d forced term amplitude ε_1, the Jupiter forced term amplitude ε_2 and other minor terms due to planetary perturbations.

For time-scales of the order of few years, we assume that Mercury is rotating around its axis of maximum momentum of inertia $\boldsymbol{Z}_2$ (no wobble). On the other hand, the formula for the rotation angle ϕ, which in general is a sum of a secular term, some periodic libration terms and a constant which depends on the choice of the zero meridian, contains only the 88 d forced libration term and the 11.9 yr forced libration term due to Jupiter. Although this last term is expected to have a small amplitude, it can experience a near-resonant amplification if its period is close to that of the free libration of Mercury. The free libration frequency is an unknown parameter, since it deeply depends on the interior model of Mercury (see e.g. Yseeboodt et al. 2013). In this paper, we assume a simple two-layers model (see Yseboodt, Margot & Peale 2010), by which the free mantle libration period is expected to be approximately 12 years, hence very close to the period of the Jupiter's perturbation on Mercury orbit. It could happen that the amplitude of this forced libration exceeds that one of ε_1. A discussion explaining why we do not include minor libration effects and the problems related to the determination of ε_2 is given in Cicalò & Milani (2012).

Explicitly, the rotation axis direction is modelled by the two angles (δ_1, δ_2), assumed to be constant over the mission time span:

$$[\boldsymbol{Z}_2]_{\rm MC_1} = (\sin\delta_1\cos\delta_2, -\sin\delta_2, \cos\delta_2\cos\delta_1)^{\rm T}.$$

Then, the obliquity η with respect to the orbit is simply given by

$$\cos\eta = \cos\delta_2\cos\delta_1\,. \qquad (5)$$

In this way, the spin direction is 'model independent', meaning that we solve-for its direction without considering any information on the Cassini state theory (Peale 2006). In this work, we will choose the reference values for the direction of the spin axis in an arbitrary way, without assuming any knowledge of the Laplace pole from the theory, leaving the interpretation of the results in terms of Laplace pole definition, as in Yseeboodt & Margot (2006), and deviation of the spin pole from the Cassini state to a future dedicated analysis.

Note that these angles are computed in the local Mercurycentric frame of reference $\Psi_{\rm MC_1}$, if we need the corresponding values in the

Barycentric frame of reference Ψ_{BC_1} we need to apply the relativistic space coordinates transformation (equations 3).

Finally, assuming the minimum momentum of inertia principal axis as zero meridian, the analytical formula adopted for ϕ is

$$\phi = \frac{3}{2} n\,(t - t_{\rm p}) + \varepsilon_1 \sin\left(n\,(t - t_{\rm p})\right) + \frac{\varepsilon_1}{\mu} \sin\left(2\,n\,(t - t_{\rm p})\right) + \varepsilon_2 \cos\left(w_{\rm j}\,(t - t_{\rm p}) + \varphi_{\rm j}\right), \quad (6)$$

where we use as reference values for the mean motion of Mercury n, the mean motion of Jupiter $w_{\rm j}$ and the time of Mercury's perihelion $t_{\rm p}$ the ones at epoch J2000, while $\varphi_j \cong -11\overset{\circ}{.}97$ and $\mu = -9.483$ depends only on the eccentricity and it is considered here as a known constant (see Jehn, Corral & Giampieri 2004). Note that we have not added any constant phase lag $\phi_0 = \phi(t_0)$ to be determined in the experiment. This is because of a rank deficiency that occurs when we try to solve also for the gravity field coefficient S_{22} (Cicalò & Milani 2012).

5.3.1 *Peale's experiment*

According to Peale (1988), the rotation state of Mercury, together with the degree two harmonic coefficients of the static gravity field, can give insightful information on the interior structure of the planet. Under suitable conditions, the obliquity of the spin-axis can be related to the maximum momentum of inertia coefficient of Mercury as a rigid body. On the other hand, the libration in longitude determination can discriminate if Mercury has a molten core decoupled from the mantle.

Assuming Mercury occupying a Cassini state 1 (Peale 2006), let $A < B < C$ the principal momenta of inertia of Mercury modelled as a whole rigid body, rotating around the axis of maximum momentum of inertia. From secular theory, the obliquity η of the spin-axis with respect to the orbit normal is given by the following formula (Peale 1988):

$$\frac{1}{\eta} = \frac{1}{\sin i_L} \left(\frac{n\,J_2\,f(e)}{w_{\rm L}} \frac{MR^2}{C} - \cos i_{\rm L} \right), \quad (7)$$

where M is the mass of Mercury, R is its mean radius, $f(e) = G_{210}(e) + 2C_{22}G_{201}(e)/J_2$, $J_2 = -C_{20}$ and C_{22} are the degree 2 potential coefficients of Mercury gravity field (in the principal of inertia body-fixed reference system), G_{210}, G_{201} are eccentricity functions defined in (Kaula 1966), n is the orbital mean motion, $i_{\rm L}$ is the inclination of the orbit with respect to its precessional axis called Laplace pole $\boldsymbol{Z}_{\rm L}$, and $w_{\rm L}$ is the nearly constant rate of the precession of the orbit around it ($2\pi/w_{\rm L} \sim 250\,000$ yr). Thus, the obliquity is directly related to the quantity C/MR^2, called the *concentration coefficient*.

If there is a core decoupled from a rigid mantle, and the core does not follow the mantle over short time-scales (while it does over long time-scales), then the momenta of inertia reacting to the torques over short time-scales are the ones of the mantle alone $A_{\rm m} < B_{\rm m} < C_{\rm m}$. In particular, assuming rotation around principal axis of inertia, the momentum which appears in the rotational kinetic energy is only $C_{\rm m}$. Then, if Mercury has a core decoupled from the rigid mantle, the ratio $C_{\rm m}/C$ is not equal to 1: for example, it is expected to be $\sim$0.5 for a planet with an important liquid layer. Current estimates from MESSENGER provide that the fractional part due to the solid outer shell is around 0.42 (Mazarico et al. 2014; Stark et al. 2015). For the concentration coefficient C/MR^2, which is, for example, 0.4 for a homogeneous planet, MESSENGER observations suggest a value around 0.35 (Mazarico et al. 2014; Stark et al. 2015). Peale proposes to determine the $C_{\rm m}/C$ ratio by the following relation:

$$\frac{C_{\rm m}}{C} = \frac{C_{\rm m}}{B - A} \frac{M\,R^2}{C} \frac{B - A}{M\,R^2}, \quad (8)$$

where MR^2/C can be measured by the obliquity, $(B - A)/MR^2 = 4\,C_{22}$ can be obtained by the harmonic coefficient C_{22}, and $C_{\rm m}/(B - A)$ can be determined by measuring the librations in longitude from the formula (Jehn et al. 2004):

$$\varepsilon_1 = \frac{3}{2} \frac{B - A}{C_{\rm m}} \left(1 - 11e^2 + \frac{959}{48} e^4 + \cdots \right). \quad (9)$$

5.4 Sun and planetary perturbations

The Solar and planetary perturbative acceleration $\boldsymbol{a}_{\rm p}$, on a satellite orbiting around Mercury, can be computed in the local Mercurycentric frame of reference as 'third-body' differential terms due to the Sun, Venus, Earth–Moon, Mars, Jupiter, Saturn, Uranus and Neptune:

$$\boldsymbol{a}_{\rm p} = \sum_{\rm bodies} GM_{\rm b} \left(\frac{\boldsymbol{d}_{\rm b}}{d_{\rm b}^3} - \frac{\boldsymbol{r}_{\rm b}}{r_{\rm b}^3} \right), \quad (10)$$

where $\boldsymbol{d}_{\rm b}$ is the position of a body (of mass $M_{\rm b}$) with respect to the satellite and $\boldsymbol{r}_{\rm b}$ is its position with respect to Mercury (see e.g. Moyer 2000; Roy 2005).

5.5 Dynamical tidal perturbations

So far we have considered the rotation of a rigid body. If we introduce an elastic component and the body is subject to some external force, then it could be deformed. This is the case for Mercury under the tidal field of the Sun. The effect is a classic tidal bulge oriented, at each instant, in the direction of the Sun. This deformation changes the expression of the Newtonian potential V (equation 4) by a quantity $V_{\rm L}$ called *Love potential* (Kozai 1965):

$$V_{\rm L} = \frac{GM_{\rm S}k_2R_{\rm M}^5}{r_{\rm S}^3 r^3} \left(\frac{3}{2} \cos^2\psi - \frac{1}{2} \right), \quad (11)$$

where $M_{\rm S}$ is the Sun's mass, $r_{\rm S}$ is the Mercury–Sun distance and ψ is the angle between the s/c Mercurycentric position $\boldsymbol{r}$ and the Sun Mercurycentric position. The Love number k_2 is the elastic constant that characterizes the effect. The MESSENGER team provides, as a preliminary estimate, the value $k_2 = 0.451 \pm 0.014$; nevertheless a wider range of values, $k_2 = 0.43$–0.50, can be reasonable (Mazarico et al. 2014).

5.6 Non-gravitational perturbations and accelerometer calibration

Being Mercury so close to the Sun, the solar radiation pressure at the planet is very high. Thus, it must be considered as a source of perturbation to the orbit of the s/c, not only its direct component on the satellite, but also the reflected radiation from the planet surface (albedo radiation pressure).

In general, modelling these non-gravitational effects is difficult, and the determination of the unknown parameters appearing in the equations is a tough problem. Trying to determine these parameters could degrade the results of the whole experiment, being the non-gravitational effects poorly modelled. As discussed in Section 3, it is possible to overcome this problem by using the on-board *accelerometer*. The accelerometer measurement $-\boldsymbol{a}_{\rm acc}$ can be used in

place of the non-gravitational acceleration $\boldsymbol{a}_{\rm ng}$, taking into account that it contains an a priori unknown error $\boldsymbol{\epsilon}$ (see Section 3.1). For this reason, we do not need to consider a detailed non-gravitational perturbation model in our simulations, since for us they are replaced by the accelerometer measurements and the main difficulty becomes the calibration of their error.

In order to simulate the on-board accelerometer measurements to be used in the least-squares fit, we consider a simplified non-gravitational model, while we focus on the implementation of a realistic measurement error model. Briefly, the direct radiation pressure $\boldsymbol{a}_{\rm rad}$ is modelled assuming a spherical satellite with coefficient 1 (that is, neglecting the diffusive term). The shadow of the planet is computed accurately, taking into account the penumbra effects. The thermal radiation from the planet $\boldsymbol{a}_{\rm th}$ is described assuming a zero relaxation time for the thermal re-emission on Mercury. In this simple setting, we do not need information about the distribution of the albedo on the Mercury's surface since it is effectively equal to 1 (this model has been supplied by D. Vokrouhlicky, Charles University of Prague). We are not including thermal thrust and other radiation pressure effects (Milani, Nobili & Farinella 1987, Chap. 5).

In this way, in the full cycle numerical simulation framework, we can compute the non-gravitational perturbations as $\boldsymbol{a}_{\rm ng} = \boldsymbol{a}_{\rm rad} + \boldsymbol{a}_{\rm th}$ in the data simulation phase, storing $\boldsymbol{a}_{\rm acc} = -\boldsymbol{a}_{\rm ng} + \boldsymbol{\epsilon}$ as simulated accelerometer measurement, with $\boldsymbol{\epsilon}$ given by a suitable model such as the one described in Section 3.1.

In principle, the error $\boldsymbol{\epsilon}$ can generate significant systematic errors in the global fit, so we must calibrate it by adding a suitable corrective term $\boldsymbol{c}$ to the accelerometer measurement $\boldsymbol{a}_{\rm acc}$, which is in principle a function of time and of a certain number of unknown parameters defining the calibration model.

The calibration model should have a qualitative behaviour similar to the error, so that it can absorb it: $\boldsymbol{c} \cong \boldsymbol{\epsilon}$ at least over some timescales. As introduced in Alessi, Cicalò & Milani (2012a) and used in Cicalò & Milani (2012), we can represent $\boldsymbol{c}(t)$ as a $\mathcal{C}^1$ Hermite cubic spline. For the whole interval going from the central time t_{k-1} of the arc $k-1$ to the central time t_k of the arc k (see Section 6.2), we represent $\boldsymbol{c}(t)$ with a cubic polynomial $\boldsymbol{c}_{k-1,k}(t)$, such that $\boldsymbol{c}_{k-1,k}(t_k) = \boldsymbol{c}_{k,k+1}(t_k) = \boldsymbol{\zeta}_k$ and $\dot{\boldsymbol{c}}_{k-1,k}(t_k) = \dot{\boldsymbol{c}}_{k,k+1}(t_k) = \dot{\boldsymbol{\zeta}}_k$. After that, we can use $\boldsymbol{a}_{\rm ng} = -\boldsymbol{a}_{\rm acc} + \boldsymbol{c}$ in the data processing phase, and the parameters to solve-for become only the ones contained in the calibration $\boldsymbol{c}$, which are $\boldsymbol{\zeta}_k$ and $\dot{\boldsymbol{\zeta}}_k$, for each arc k. Plus the boundary conditions, six associated with the first observation time and six with the last one.

Note that this calibration model can be useful to absorb only low-frequency error terms, while the high-frequency components are left uncalibrated and in principle can still be responsible for large systematic errors.

5.7 Manoeuvres

Additional sources of perturbation on the orbit of the s/c around Mercury are the manoeuvres performed on it. In particular, the reaction wheels desaturation manoeuvres. A detailed discussion on this problem is given in Alessi et al. (2012b), according to which, under suitable hypothesis, it is possible to add the velocity change $\Delta\boldsymbol{v}$ due to each manoeuvre to the list of solve-for parameters. We will assume as a general scenario to have one dump manoeuvre during tracking and one dump manoeuvre in the 'dark' periods without tracking, hence a maximum amount of two dump manoeuvres per arc (see Section 6.2), as specified in the mission requirements. The presence of orbital manoeuvres, which are in general much larger than the desaturation manoeuvres, is not considered here. The values for the $\Delta\boldsymbol{v}$ used in the simulation, along with all the details on the modelization and implementation of the manoeuvres scenario are given in Alessi et al. (2012b).

5.8 Relativistic corrections

According to Huang et al. (1990), also reported in Moyer (2000), for the case of a near-Earth spacecraft in a geocentric frame of reference, once we have performed the relativistic space–time transformation of coordinates of equation (3) and we are considering the dynamics of a near-Mercury spacecraft in the local Mercurycentric frame of reference, the relativistic perturbative acceleration is obtained from the one-body Schwarzschild isotropic metric for Mercury:

$$\boldsymbol{a}_{\rm rel} = \frac{GM}{c^2 r^3}\left\{\left[2(\beta+\gamma)\frac{GM}{r} - \gamma\,\boldsymbol{v}\cdot\boldsymbol{v}\right]\boldsymbol{r} + 2(1+\gamma)(\boldsymbol{r}\cdot\boldsymbol{v})\boldsymbol{r}\right\},$$

where β and γ are classic post Newtonian parameters, and c is the speed of light, plus the acceleration due to geodesic precession:

$$\boldsymbol{a}_{\rm prec} = 2\frac{GM_{\rm S}(\gamma+\frac{1}{2})}{c^2 r_{\rm S}^2}(\boldsymbol{r}_{\rm S}\times\boldsymbol{v}_{\rm S})\times\boldsymbol{v},$$

being $\boldsymbol{r}_{\rm S}$, $\boldsymbol{v}_{\rm S}$ the Mercurycentric position and velocity of the Sun, respectively.

6 NUMERICAL SIMULATION SETTINGS

In order to test the feasibility of the gravimetry and rotation MORE experiment, we set up a full cycle numerical simulation using the orbit determination and parameter estimation software ORBIT14, developed by the Celestial Mechanics group of the University of Pisa, Department of Mathematics, under ASI contract. In this section, we will describe all the main features and settings of the numerical simulations. Also in Alessi et al. (2012b) and Cicalò & Milani (2012) analogous simulations were performed. However, in this work we will take into account more recent and realistic error models for the tracking and the on-board accelerometer measurements and we will include the on-board camera observations. We will see that these updated error models are significant in affecting the scientific results, and much care must be taken in considering them. Moreover, more realistic assumptions for the mission time span and for the tracking sessions available are considered here (see Section 8).

The main programs used to perform the numerical simulation belong to two categories: data simulator and differential corrector. The simulator generates simulated observables (range and range-rate, accelerometer readings, optical measurements) and preliminary orbital elements. The corrector solves for all the parameters which can be determined by a least-squares fit (possibly constrained and decomposed in a multi-arc structure, see Section 6.2).

Because of the multiple dynamics upon which the observables depend, the main programs need to have the propagated state available for each dynamics (for the list of dynamics, see Section 2). This is obtained in different ways, depending upon the dynamics. For the dynamics which have to be propagated by numerical integration, that is the Mercurycentric orbit of the s/c and the Solar system orbits of Mercury and the EMB, we call a propagator which solves the equation of motion, for the requested time interval. The states (time, position, velocity, acceleration, etc.) are stored in a memory stack, from which interpolation is possible with the required accuracy. Then, when the state is needed to compute the observables range/range-rate, the dynamics stacks are consulted and interpolated. In the case of the Earth rotational dynamics,

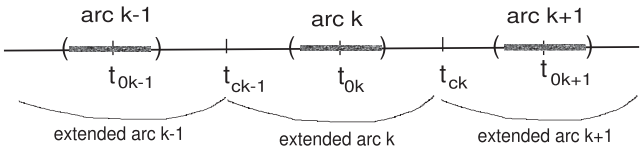

Figure 5. Temporal structure of the observed arcs and extended arcs.

the Earth orientation data can be downloaded from the International Earth Rotation Service website http://www.iers.org,[6] and used for interpolation. For the other planets and the Earth–Moon system, planetary ephemerides are consulted from the Jet Propulsion Laboratory DE421 version, which can be downloaded from the http://ssd.jpl.nasa.gov/[7] website.

6.1 Least squares

Here we introduce the main definitions and notations for the least-squares method, to be applied in the simulated data processing (Milani & Gronchi 2010, Chap. 5 and 6). Let $\boldsymbol{\xi}(\boldsymbol{X}) = \mathcal{O} - \mathcal{C}(\boldsymbol{X})$ be the residuals, i.e. the differences between the observations and the corresponding computed values, and let $\boldsymbol{X}$ be the parameters which affect the dynamical and observation model and that we want to determine. The target function Q to minimize is a quadratic form in $\boldsymbol{\xi}$:

$$Q(\boldsymbol{\xi}(\boldsymbol{X})) = \frac{1}{m}\boldsymbol{\xi}^{\mathrm{T}} W \boldsymbol{\xi} = \frac{1}{m}\sum_{i=1}^{m}\sum_{k=1}^{m} w_{ik}\xi_i\xi_k \ ,$$

where m is the number of observations, $W = (w_{ik})$ is the *weight matrix*, a symmetric matrix with non-negative eigenvalues used to weight the residuals. The minimum $\boldsymbol{X}^*$ of the target function is then found by an iterative *differential corrections* method:

$$\boldsymbol{X}_{k+1} = \boldsymbol{X}_k - C^{-1}\boldsymbol{\xi}_X^{\mathrm{T}} W \boldsymbol{\xi},$$

where $C = \boldsymbol{\xi}_X^{\mathrm{T}} W \boldsymbol{\xi}_X$ is the *Normal matrix* and $\boldsymbol{\xi}_X = \partial\boldsymbol{\xi}/\partial\boldsymbol{X}$. We always use the probabilistic interpretation of its inverse $\Gamma = C^{-1}$, as the *covariance matrix* of the vector $\boldsymbol{X}$, considered as a multivariate Gaussian distribution with mean $\boldsymbol{X}^*$ in the space of parameters.

6.2 Pure and constrained multi-arc strategy

We call an *observed arc* each set of range and range-rate tracking data, separated from the next one by several hours because of the visibility conditions of the s/c from the Earth (typically one set per day). Between two subsequent observed arcs we have a 'dark' period without tracking. We define an *extended arc* an observed arc extended from half of the dark period before it to half of the dark period after it. In this way two subsequent extended arcs have one connection time (Fig. 5). During the ORBIT14 development phase, we fixed a requirement on the number of dump manoeuvres, that is with the constrained multi-arc strategy we are able to handle not more than two manoeuvres per arc, one during tracking and one in the dark. Finally, an *orbital arc* is a sequence of causally connected subsequent extended arcs. Two subsequent orbital arcs are separated by a dark period significantly longer than one day, in which several manoeuvres can take place; thus, it is not possible to solve for all these manoeuvres and two different orbital arcs have to be considered as not causally connected.

As in Alessi et al. (2012b) and Cicalò & Milani (2012), we will adopt a *multi-arc strategy* to process the data, and we can classify the solve-for parameters in different categories: *global parameters*, *local parameters* and *local external parameters*, depending on the arcs they affect. In the case of the BepiColombo mission to Mercury, the problem is affected by the symmetries and rank deficiency described in Bonanno & Milani (2002), thus considering that the observed arcs are not causally connected would lead to a weak and unstable orbit determination. However, exploiting the fact that each observed arc belongs to the same object (the s/c), we can add information by considering that at the connection times between two subsequent extended arcs the orbits should coincide. This technique is defined in Alessi et al. (2012b), and it is called *constrained multi-arc strategy*. In particular, in this paper we use the a priori constrained technique, which consists in constraining by a fixed quantity the discrepancies, in positions and velocities, of the propagation of two subsequent arcs at their connection time.

The total target function is defined as

$$Q = \frac{1}{m+6(n-1)}\sum_{k=1}^{n}\boldsymbol{\xi}^k\cdot W_k\boldsymbol{\xi}^k + \frac{1}{m+6(n-1)}\sum_{k=1}^{n-1}\boldsymbol{d}^{k,k+1}\cdot C_{k,k+1}\boldsymbol{d}^{k,k+1}, \quad (12)$$

where m is the total number of observations, n is the total number of observed arcs, W_k are the weight matrices of the observations, assumed to be diagonal with entries of the form $1/\sigma^2$, where σ is given for each observation from the error model of Section 2.2. Finally, $\boldsymbol{d}^{k,k+1}$ are the discrepancy vectors defined in Alessi et al. (2012b) along with their weight matrices (units are cm for positions and cm s^{-1} for velocities):

$$C_{k,k+1} = \mu^{-1}\,\mathrm{diag}(1, 1, 1, 10^6, 10^6, 10^6).$$

The value of μ can be properly chosen in order to have more smoothness at the connection times, for our purposes a choice of $\mu = 1$ turns out to be appropriate.

7 ASSUMPTIONS ON THE SIMULATION SCENARIO

In this section, we describe the dynamical and observational scenario that we assume for the numerical simulations of the radio science experiment. We shall define a nominal scenario, as a reference point for further tests, and three variations from it, in terms of error and observational models. In all these cases, the error models of the observable quantities contain not only random errors, but systematic errors as well, the latter being more important to determine the true accuracy of the results, as opposed to the formal accuracy. Thus, the most complete error budget contains the effect of systematic measurement errors and is more reliable than a formal one.

The nominal simulation scenario is described with the following list:

(i) 365 d simulation time span, starting on 2024 April 10, at 19:00 UTC (this is the actual estimate for the beginning of scientific operations);

[6] McCarty D. D., Petit G. (eds); 2003; IERS Conventions (2003), IERS Technical Note n. 32, Verlag des Bundesamts fur Kartographie und Geodasie, Frankfurt am Main, Germany, ISBN 3-89888-884-3.
[7] Folkner W. M., Williams J. G., Boggs D. H., The planetary and Lunar Ephemerides DE421, JPL Interoffice Memorandum IOM 343.R-08-003.

(ii) two ground stations available for tracking, one in *X* band (in Madrid, Spain) and one in *Ka* band (in Goldstone, CA): an average of 15 h per day of tracking, of which eight in *Ka* band. Range measurements are taken every 120 s, while range-rate measurements every 30 s. Gaussian and systematic errors added to tracking observables are described in Section 2.2;

(iii) optical observations from the high-resolution on-board camera are included in the simulations an average of two observations per arc, with a standard deviation of 2.5 arcsec, assuming a geodetic reference network on Mercury surface of 100 reference points randomly distributed in longitude and at fixed latitudes between -60° and $+60^\circ$;

(iv) the gravity field spherical harmonics are simulated up to degree $l_{\max} = 25$: we assume as nominal gravity field of Mercury the one estimated by Messenger (Mazarico et al. 2014);

(v) the Sun tidal effects are described by the Love number k_2 (to define the parameter k_2, we followed the description given for the Earth in Kozai 1965);

(vi) the semi-empirical model introduced in Section 5.3 is considered: the rotation parameters are the two angles δ_1 and δ_2, defining the *obliquity* of Mercury spin axis; ε_1, the *amplitude of librations in longitude* at Mercury orbital period and ε_2, the 11.9 yr Jupiter near-resonant libration term;

(vii) the solar radiation pressure and the indirect Mercury albedo radiation pressure are included in the simulation of the observables as discussed in Section 5.6, and used to generate simulated on-board accelerometer measurements with the addition of the error described in Section 3.1;

(viii) in the least-squares fit of the simulated observations, the non-gravitational effects are assumed as read by the on-board accelerometer which is always on. The measurements are calibrated by the cubic spline technique described in Section 5.6;

(ix) two dump manoeuvres are performed for each arc, one during tracking and one in the dark period between two subsequent arcs, see Section 5.7. We assume that the manoeuvres do not affect the accelerometer readings, while, in reality, the accelerometer data during a dump manoeuvre have to be discarded;

(x) the strategy used to process the simulated observations is the a priori correlated-constrained multi-arc method, as defined in Section 6.2, with $\mu = 1$.

In general, we aim at discussing two fundamental issues, which are, on one side, to evaluate the possible benefits, especially for the rotation experiment, arising from including camera observables in addition to tracking data, while, on the other side, to quantify the expected deterioration of the solution due to the systematic effects unavoidably present in the accelerometer readings. To handle these two effects individually and in order to improve our understanding of the BepiColombo radio science experiment, we performed a sensitivity study, defining three other simulation scenarios, as summarized in the following test cases.

(i) *Test case 1*: nominal scenario;

(ii) *Test case 2*: nominal scenario without on-board camera observations;

(iii) *Test case 3*: nominal scenario with 5 arcsec on-board camera error (see Section 4.3);

(iv) *Test case 4*: nominal scenario with low-frequency random rise added in the accelerometer error model (see Section 3.1).

The correction step is always defined by the following list of solve-for parameters:

Global dynamical:

(i) Coefficients of the (normalized) spherical harmonics of the gravity field of Mercury, static part; degree from 2 to 25, all possible orders.

(ii) Dynamical Love number k_2.

(iii) Rotation parameters δ_1, δ_2, ε_1, ε_2. As extensively discussed in Cicalò & Milani (2012), there is a potential rank deficiency between ε_2 and S_{22} depending on the choice of the mission time epoch and duration. From simulations with tracking data alone, it turns out that with the current choice of mission epoch the correlation between the two parameters is very close to 1, even if in this work, differently from Cicalò & Milani (2012), we are considering 1 yr time span simulations instead of 88 d. In Test case 2, the nominal scenario without camera, an alternative approach could be not to determine ε_2, assuming a good considered value from the theory, and absorbing possible residual errors with the S_{22} static gravitational parameter determination. We will see that, eventually, the joint combination of radiometric and optical observations mitigates the problem, lowering significantly the correlation between the two parameters.

(iv) Six accelerometer calibration constants $(\boldsymbol{\zeta}_k, \dot{\boldsymbol{\zeta}}_k)$, for each arc, plus 6+6 boundary conditions.

Local dynamical:

(i) six initial conditions, Mercurycentric position and velocity in the Ecliptic J2000 inertial frame, at the central time of each observed arc;

(ii) three dump manoeuvre components, taking place during tracking, for each observed arc.

Local external dynamical:

(i) three dump manoeuvre components, taking place in the dark period between each pair of subsequent observed arcs.

8 GRAVIMETRY AND ROTATION EXPERIMENT RESULTS

All the results presented in this section are intended to be at convergence of the differential corrections process. The analysis is performed both on formal statistics (standard deviations and correlations), as given from the formal covariance matrix $\Gamma = C^{-1}$, and on the actual (true) errors, defined as the difference between the parameters value at convergence and the value used in the simulation of the observables. Due to the presence of systematic components in the tracking and accelerometer error models (Section 3.1), the true error represents an estimate of the 'real' accuracy we can expect for the associated parameter including systematic errors. However, a single realization of the random component of the tracking and accelerometer errors during a simulation could not be enough to give a reliable indication of this accuracy. For this reason, several realizations of the same experiment have been performed, varying only the random component of the simulated errors (tracking, camera and accelerometer). The formal statistics is not affected by the variation of the errors, but the true errors can significantly oscillate. A reference value for the true errors is then obtained computing the root mean square of the errors obtained in each realization (a number of $\sim$10 realizations turned out to be enough to stabilize this value).

Note that, once a formal standard deviation (formal uncertainty) is associated with each parameter from the matrix Γ (Section 6.1), the convergence of the differential corrections can be tested by adding an error significantly larger than the formal uncertainty to each parameter first guess.

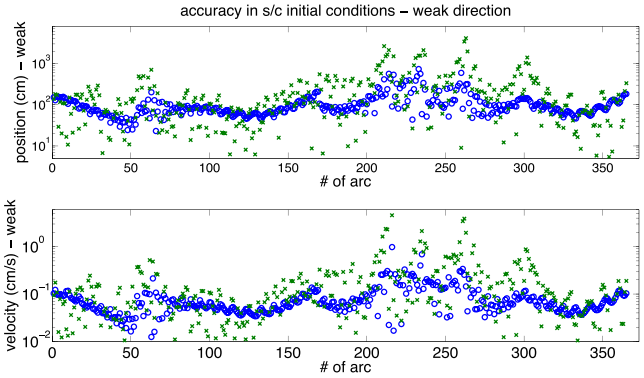

Figure 6. Spacecraft initial conditions, positions (top panel) and velocities (bottom panel), along weak direction: formal (circles) and true (crosses) uncertainties.

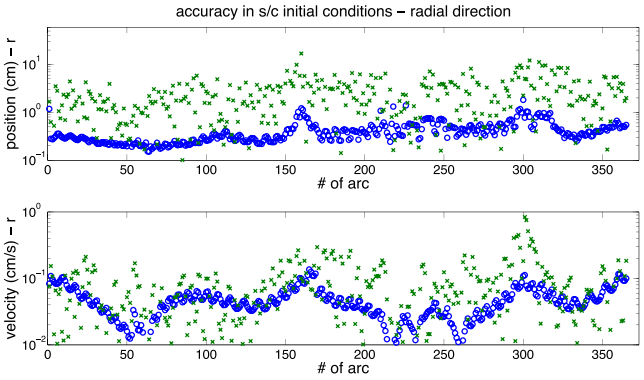

Figure 7. Spacecraft initial conditions, positions (top panel) and velocities (bottom panel) along radial direction: formal (circles) and true (crosses) uncertainties.

More precisely, the results can be described in terms of s/c initial conditions determination, gravity field and rotation state determination, surface geodetic network determination, accelerometer error calibration and desaturation manoeuvres. As defined in the previous section, we have considered a total of four main Test cases. The main significant variations in the results of these different cases turned out to be in the rotation state determination, with the only exception of the S_{22} coefficient of the gravity field, whose accuracy depends on the scenario due to the high correlation with the ε_2 parameter. All the results presented in Sections 8.1 and 8.2 are from the nominal scenario, while in Section 8.3 we will focus on the differences, especially in the rotation state determination, arising from considering the four Test cases.

8.1 Spacecraft initial conditions

In the following, we show the results for the determination of the Mercurycentric position and velocity of the spacecraft over time (we remind that we determine the Mercurycentric coordinates of the s/c at the central time of each arc). Fig. 6 shows the results along the weak direction (as defined in Section 2.2), while in Fig. 7, we plot the results for the radial direction: the formal (circles) and true (crosses) uncertainties in the position and velocity determination are shown in the top and bottom panel of each figure, respectively. As it can be seen, for each direction the general behaviour is that true errors are higher than formal ones. Moreover, while the expected accuracy in position along the radial direction is still around the cm

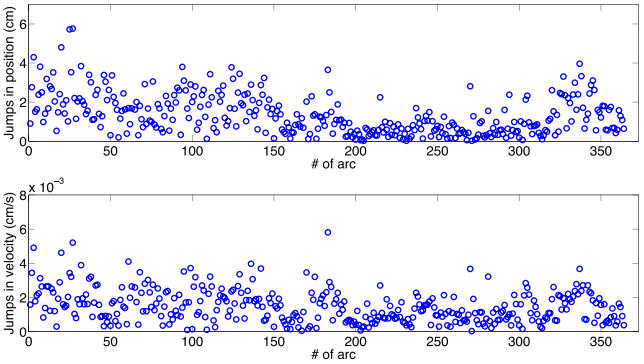

Figure 8. Discrepancies in position (cm) and velocity (cm s^{-1}) between two subsequent arcs initial conditions propagated at the same time.

level, along the weak direction it is expected to be almost two orders of magnitude worse, implying that the s/c Mercurycentric orbit can be determined at the level of some metres.

The reason of the general deterioration of true accuracies with respect to formal ones can be found in the accelerometer systematic errors, which are not completely absorbed by the calibration process. Indeed, we checked that removing the systematic part of the accelerometer error model, i.e. adding only Gaussian noise, true and formal accuracies are comparable.

In Fig. 8, we show the discrepancies in positions and velocities between two subsequent arcs initial conditions propagated at the same central time. As expected by the constrained multi-arc technique (see Section 6.2) with $\mu = 1$, the discrepancies are forced by the a priori constraints to be at the cm level in positions and 10^{-3} cm s^{-1} level in velocities.

8.2 Gravity field

We estimated the normalized harmonic coefficients $\bar{C}_{\ell m}$ and $\bar{S}_{\ell m}$ up to degree $\ell = 25$, related by the ones defined in equation (4) by

$$\bar{C}_{\ell m} = \frac{C_{\ell m}}{H_{\ell m}}, \quad \bar{S}_{\ell m} = \frac{S_{\ell m}}{H_{\ell m}},$$

with

$$H_{\ell m} = \sqrt{(2\ell+1)(2-\delta_{0m})\frac{(\ell-m)!}{(\ell+m)!}},$$

where $\delta_{0m} = 1$ for $m = 0$, $\delta_{0m} = 0$ otherwise.

To evaluate in a simple and immediate way the accuracy of the gravity field determination, we consider together the contribute of each harmonic coefficient for a given degree ℓ:

$$\bar{C}_\ell = \sqrt{\frac{\sum_{m=0}^{\ell}(\bar{C}_{\ell m}^2 + \bar{S}_{\ell m}^2)}{2\ell+1}}$$

and we compare it with the corresponding value from Kaula rule (Kaula 1966). We show the results in Fig. 9, where we plot the behaviour of the $\bar{C}_\ell$ coefficients over ℓ (labelled as simulated field from MESSENGER), and the corresponding Kaula rule. The true error for each degree has been obtained as rms sum of the true errors of each $\bar{C}_{\ell m}$ and $\bar{S}_{\ell m}$ coefficient for a given degree ℓ and similarly for formal standard deviations. Finally, we show also the rms MESSENGER uncertainty for comparison (see Mazarico et al. 2014). Comparing true error with the simulated field, we point out that the signal-to-noise ratio is still a factor of 10 at degree 25.

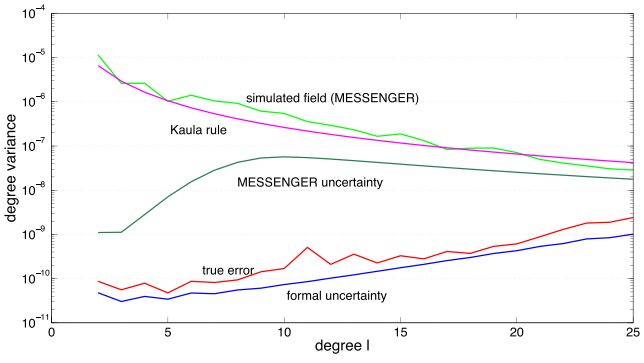

Figure 9. Global gravity field of Mercury: (from top to down) simulated nominal field (from MESSENGER), Kaula rule, MESSENGER uncertainty, actual error, formal uncertainty.

As it can be seen, the ratio between the formal uncertainties and the true errors is higher than 1, especially for some degree ℓ: as in the case of initial conditions determination, this systematic effect reflects the non-calibrated contribute of accelerometer readings. In particular, it is due to the error component at s/c orbital period (see Section 3.1): in fact, the $\mathcal{C}^1$ spline calibration provides the estimate of two parameters (value and first derivative) per arc per direction, hence it can absorb almost completely the Mercury sidereal period components of ISA noise model, but not the probe orbital period component, which has a periodicity significantly shorter.

This has been verified by additional simulations, in which the probe orbital period term was removed from the accelerometer error model: in such a case, the true to formal error ratio lies around unity. As already stated in Section 3.1, varying the amplitude of the orbital period component, especially for the along-track direction, significantly changes the results for the achievable gravity field accuracy.

This fact highlights that the gravimetry experiment (and also the rotation experiment) is deeply related to the accelerometer error model, especially concerning the probe orbital period term. Since the provided error model cannot be considered the final one, we cannot give a complete conclusion on the expected accuracy on gravity field determination. The depicted scenario is the one we expect if the accelerometer behaviour is not far from the current error model.

Table 1 shows formal standard deviations, true errors and true to formal error ratio for each normalized harmonic coefficient of degree $\ell = 2$. These results can be compared with the ones found after three years of radio tracking data from MESSENGER (Mazarico et al. 2014): for each $\ell = 2$ coefficient MORE is expected to improve the accuracy by at least one order of magnitude.

Finally, in Table 2 the results for the determination of the Love number k_2 are given. The expected accuracy for k_2 can be compared with the current estimate from the MESSENGER mission. As a preliminary result, the analysis of MESSENGER radio tracking data has led to the solution $k_2 = 0.45 \pm 0.014$ (Mazarico et al. 2014); the formal and true accuracies provided by our simulations are almost two orders of magnitude better, hence even assuming a 3σ confidence level, we can expect to improve the knowledge on k_2 with BepiColombo by at least one order of magnitude.

Table 1. Order $\ell = 2$ (normalized) harmonic coefficients determination.

Coefficient	Formal	True	True/Formal
$\bar{C}_{20}$	3.5×10^{-11}	4.1×10^{-11}	1.2
$\bar{S}_{21}$	2.0×10^{-11}	2.3×10^{-11}	1.1
$\bar{C}_{21}$	2.0×10^{-11}	2.3×10^{-11}	1.1
$\bar{S}_{22}$	7.9×10^{-11}	7.9×10^{-11}	1.0
$\bar{C}_{22}$	5.3×10^{-11}	1.5×10^{-10}	2.8

Table 2. Love number k_2 determination result.

Parameter	Formal	True	True/Formal
k_2	2.4×10^{-4}	3.8×10^{-4}	1.6

Table 3. Rotational parameters results (δ_1, δ_2 in arcmin, ε_1, ε_2 in arcsec) in the four Test cases: nominal, no camera, camera with 5 arcsec Gaussian error, random rise in accelerometer error model.

Parameter	Formal	True	True/Formal
Test case 1		Errors	
δ_1 [arcmin]	0.0008	0.0011	1.4
δ_2 [arcmin]	0.0005	0.0013	2.6
ε_1 [arcsec]	0.047	0.11	2.3
ε_2 [arcsec]	0.57	0.69	1.2
Test case 2			
δ_1 [arcmin]	0.0013	0.0014	1.1
δ_2 [arcmin]	0.0007	0.0019	2.7
ε_1 [arcsec]	0.13	0.75	5.7
ε_2 [arcsec]	1.7	2.8	1.6
Test case 3			
δ_1 [arcmin]	0.0011	0.0013	1.2
δ_2 [arcmin]	0.0006	0.0015	2.5
ε_1 [arcsec]	0.079	0.31	3.9
ε_2 [arcsec]	0.98	1.3	1.3
Test case 4			
δ_1 [arcmin]	0.0008	0.0015	1.9
δ_2 [arcmin]	0.0005	0.0015	3.0
ε_1 [arcsec]	0.047	0.14	3.0
ε_2 [arcsec]	0.57	0.84	1.5

8.3 Rotation state

In this section we show the results for the rotation state determination, in terms of direction of the spin-axis and forced librations in longitude amplitudes. Differently from all the other solve-for parameters results, the rotation state determination turned out to be significantly affected by the assumptions of the four Test cases introduced in Section 7. The results of the four Test cases are gathered in Table 3, where it is shown the formal uncertainty, the true error and the true to formal error ratio in the determination of δ_1, δ_2, ε_1 and ε_2 parameters.

A first important thing to note is that the ε_1 parameter is by far the most affected by the systematic errors of the accelerometer, even in the nominal case, where the low-frequency random rise component of the accelerometer error model has been removed. This effect is mainly due to the resonant term of the ISA error: this fact has been verified by removing also this component and checking that in such a case the true to formal error ratio lies around unity. Moreover, comparing test case 4 with the nominal one, it is clear that the low-frequency random rise component contributes in worsening the results also for δ_1 and δ_2. Secondly, the use of the on-board camera proved to be useful in significantly improving the rotation state determination with respect to the case without on-board camera measurements (Test case 2); this fact is more evident if the camera error is at the 2.5 arcsec level (Test case 1), providing

an improvement, comparing formal sigmas, of a factor of almost 2 considering the obliquity angles, and a factor of ∼3 for the libration amplitudes. Assuming an error at the 5 arcsec level (test case 3), the results are still more accurate than the ones obtained with radio tracking measurements only (test case 2), but in a less significant way.

We can compare the expected accuracies from our simulations with the current knowledge on the Mercury rotation state. From MESSENGER radio tracking data, Mazarico et al. (2014) obtained an obliquity of $\eta = 2.06 \pm 0.16$ arcmin, entirely consistent within half a standard deviation, with the Margot et al. (2012) estimate of $\eta = 2.04 \pm 0.08$ arcmin, obtained by Earth-based radar measurements. Lately, the result has been further confirmed by Stark et al. (2015), who obtained the value $\eta = 2.029 \pm 0.085$ arcmin, by making use of both orbital image and laser altimeter data acquired by MESSENGER. Considering the true accuracies expected for the δ_1 and δ_2 angles in the less favourable case of our simulations (Test case 2), it turns out that the MORE experiment can still significantly improve the knowledge on the obliquity, possibly by more than one order of magnitude. Concerning the amplitude of the librations in longitude at 88 d, the estimate from Margot et al. (2012), which provide the value $\varepsilon_1 = 38.5 \pm 1.6$ arcsec, has been recently improved by MESSENGER (Stark et al. 2015) to $\varepsilon_1 = 38.9 \pm 1.3$ arcsec. Comparing this result with the true accuracy provided by Test case 2, we can conclude that BepiColombo can still improve the actual knowledge, but likely by less than one order of magnitude, depending on the accelerometer behaviour.

As outlined in Section 5.3.1, the obliquity and the amplitude of the librations in longitude can provide information on the interior structure of the planet, as they are linked with the C/MR^2 and C_m/C coefficients, respectively. Constraining these parameters values is one of the main goals of the BepiColombo radio science experiment, since their geophysical interpretation will provide unprecedent information on Mercury's interior. Only with real data, we will be able to give a realistic constraint on these geophysical quantities, here we can only make some considerations on the expected accuracies. The current knowledge of C/MR^2 (relative accuracy) from MESSENGER is at 4 per cent level from radio tracking data (Mazarico et al. 2014) and at 3 per cent level from combination of laser altimetry and imaging data (Stark et al. 2015), the main error source being the uncertainty in the obliquity knowledge. An order of magnitude estimate of the obliquity accuracy which can be achieved with the MORE experiment can be computed by considering the formal accuracies in δ_1 and δ_2 angles from Test Case 2 (the worst case, since no camera observations are added): in such a case, we can still expect to improve the knowledge in the obliquity relative accuracy by one order of magnitude, which can provide a significant improvement in the concentration coefficient knowledge. An approximate estimate on the achievable accuracy in the C_m/C coefficient can, instead, be inferred by considering the relative accuracy in the ε_1 parameter, assuming the true accuracy in the worst case (Test case 4), which is still below the 2 per cent level. This value can be compared with the current relative uncertainty of 5 per cent found in Mazarico et al. (2014) and Stark et al. (2015).

Finally, regarding the ε_2 parameter, we have already noticed that, in the current mission scenario, a very high correlation with the S_{22} spherical harmonics coefficient deteriorates the solution for both parameters if only tracking data were used. Indeed, in Test case 2, we have a correlation $\varrho(\varepsilon_2, S_{22}) \sim 0.97$, and the ε_2 formal sigma is worse than in the nominal case by a factor of 3. Moreover, the S_{22} formal uncertainty is worsen by more than a factor of 2. Considering, instead, the Test cases 1 and 4, where camera observations

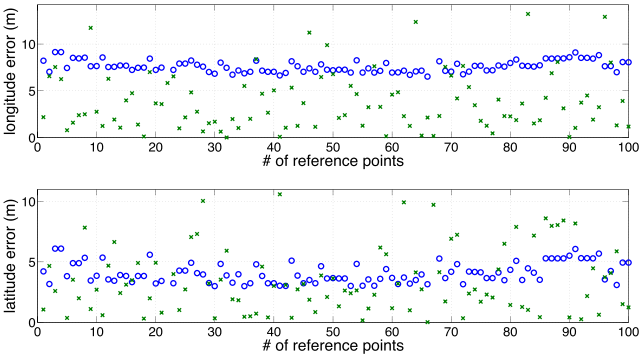

Figure 10. Formal (circles) and true (crosses) uncertainties in the determination of longitude (top panel) and latitude (bottom panel) for each reference point, expressed in terms of spatial resolution on the surface.

with a 2.5 arcsec Gaussian error are added, we find a much lower correlation $\varrho(S_{22}, \varepsilon_2) \sim 0.80$, and in this case the solution for both parameters is improved significantly.

It is worth noting that, if we change the interior model (e.g. Yseeboodt et al. 2013), the free libration period can change significantly, and then the resonance with the planetary forced terms could be either absent or resonant with another planet's period (e.g. Saturn's ∼14 yr period). Moreover, the possibility to reliably discriminate a resonant forced libration term would improve the constraint on the free libration period, and thus on the interior structure of the planet. The consequences of these aspects will be addressed in a future dedicated work.

8.4 Geodetic network

As a byproduct of the rotation experiment with the on-board camera, we obtain an accurate determination of the positions of the observed reference points on the surface of Mercury. Fig. 10 shows the formal accuracies and the true errors in the determination of longitude and latitude of the reference points, expressed in terms of spatial resolution on the planet surface. The figure refers to the nominal case (Test case 1), where a standard deviation of 2.5 arcsec is assumed as pointing error. In such a case, the position on the surface of each reference point is below the arcsec level both in latitude and longitude; in terms of spatial resolution on the planet surface we find a formal accuracy of 4–5 m in latitude and 7–8 m in longitude. The higher values for longitude formal uncertainties is due to a component of rigid rotation of the network. It is possible to eliminate this systematic error by fixing the longitude of one of the reference points, as normally done in the definition of cartographic coordinates. In such a way, accuracy in longitude and latitude can be comparable.

Moreover, assuming a 5 arcsec standard deviation for the camera observations (Test case 3), it follows that we would lose a factor of 2 in the accuracy of the reference points position, but we would still determine the geodetic network with a spatial accuracy not exceeding the 10 m level resolution. We can conclude that in the less favourable case of 5 arcsec standard deviation, even if the camera does not produce a significant improvement in the determination of the rotation parameters, it is still extremely useful for an accurate determination of the reference geodetic network.

8.5 Accelerometer error calibration

As detailed in Section 5.6, we make use of a C^1 spline model to calibrate the accelerometer readings, determining two parameters

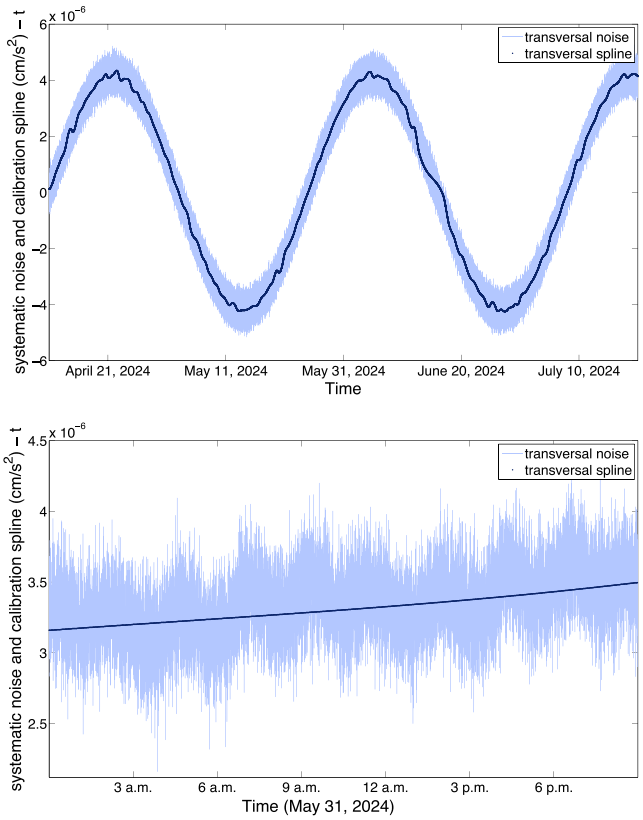

Figure 11. Polynomial spline calibration (thin curve) of the accelerometer error (large curve) over the first 100 d of simulation (top) and, as an illustrative case, a zoom of the same curves over a single day (bottom).

per arc per direction. This approach lies on the idea of a conceptual separation between the frequencies we need to calibrate and the accelerometer measurement bandwidth, hence determining only two calibration parameters per direction per arc allows us to account for the low-frequency systematic components, i.e. for the terms with a periodicity of one day or higher. On the other hand, considering the up-to-date error model, described in Section 3, the problem arises from the fact that there is a significant high-frequency component, with a periodicity of about 2 h (the s/c orbital period), which is the same periodicity of the signal. In principle, we could think of increasing the number of calibration parameters per arc to account for lower frequencies components; nevertheless, such an approach would significantly degrade the global solution. When dealing with real data, the situation will be different: we could perform a rough calibration of the orbital period term by simply introducing in the list of global solve-for parameters the amplitude and phase of a sine function at s/c orbital period. However, this could be misleading at the simulation stage since the error model provides exactly a sine function at the probe orbital period, hence we would underestimate the effect of this component. In conclusion, we assumed to deal with a residual term at orbital period with amplitude 1×10^{-7} cm s^{-2}, without applying any further calibration to it. As a consequence, the non-calibrated component at s/c orbital period together with the residual effects after calibration at lower frequencies cause the true errors to be, in general, worse than formal ones. Fig. 11 shows, on the top panel, how the spline calibration is efficient in absorbing the low-frequency systematic component of the accelerometer error in the orbit transversal direction, which is the most critical one. In the bottom panel of Fig. 11 we, instead, show a zoom of the top panel over a single day, to underline how the calibration is completely insensitive to the high-frequency periodic component (2.5 h) of the error model. The calibration in the radial direction is about one order of magnitude less accurate than in the transversal one, while that in the out-of-plane direction turns out to be even worse, but their contribution is of minor importance in the accumulation of systematic errors in the orbit.

8.6 Desaturation manoeuvres

The results for the determination of the desaturation manoeuvres can be summarized just stating that the formal accuracies obtained are analogous to the ones given in Alessi et al. (2012b, a priori case). In our present simulation results, these quantities are very much affected by systematic errors coming from the lack/inaccuracy of the accelerometer calibration model. The true error dominates the formal uncertainty up to an order of magnitude in several cases. However, even in the worst cases, the error does not exceed of the order of $\sim 10^{-2}$ cm s^{-1}, and a relative accuracy of the order of few per cent of the nominal value.

9 CONCLUSIONS

In this work, we have presented the results of a global full cycle simulation of the MORE gravimetry and rotation experiments, carried out in an up-to-date 1 yr mission time span scenario, including both radio tracking observables and optical observables from the on-board high-resolution camera, and an updated accelerometer error model. All the computations were performed with the ORBIT14 software, developed by the Celestial Mechanics Group of the University of Pisa Mathematics Department. The first full cycle simulations of the MORE experiments were performed by our group in 2001 (see Milani et al. 2001) aiming at defining the instruments performances and requirements needed to achieve the scientific goals. More recently, specific aspects of the experiment were investigated in Alessi et al. (2012a,b) and Cicalò & Milani (2012). At present time, the instruments have already been assembled but some issues are still open, as the performances of the on-board accelerometer and the thermomechanical stability. It will be possible to definitively test them only during the cruise phase.

The main aim of this work was not to dictate mission requirements because it is too late, and not even to predict the results of the real experiment. The most useful contribution of our simulations is to allow us to identify the critical elements of the BepiColombo radio science experiment, in order to be able to find suitable solutions in advance.

The results can be stated in terms of s/c initial conditions determination, gravity field and rotation parameters estimation, on-board accelerometer calibration, desaturation manoeuvres and surface geodetic network determination. The formal uncertainties were compared with true errors between simulated and estimated values. The results of the full cycle simulation are good and encouraging: the experiments are feasible at the required level of accuracy provided that some critical terms in the on-board accelerometer error are moderated. Finally, the contribution of the on-board camera to the rotation experiment would be significant only if the pointing error will be around 2.5 arcsec. If the error will be a factor of 2 higher, the camera will still be useful in the determination of the geodetic network of reference points.

We have underlined the advantages of a joint use of tracking and optical observations: the rotation experiment can significantly

benefit from the camera observables providing that the angular resolution accuracy corresponds to the requirements. On the other hand, all the expected accuracies are deeply related to the accelerometer behaviour, hence, dedicated in-flight calibration test sessions are necessary during the cruise phase.

ACKNOWLEDGEMENTS

The results of the research presented in this paper have been performed within the scope of the contract ASI/2007/I/082/06/0 with the Italian Space Agency. The authors are particularly thankful to the University of Rome 'La Sapienza' and the University of Bologna-Forlì Radio Science teams, for their precious support in the validation and testing of the ORBIT14 software.

REFERENCES

Alessi E. M., Cicalò S., Milani A., 2012a, in Guerman A. D., Bainum P. M., Contant J.-M., 1st IAA Conf. Vol, 145, Advances in the Astronautical Sciences. Am. Astronaut. Soc. Univelt, CA, p. 121
Alessi E. M., Cicalò S., Milani A., Tommei G., 2012b, MNRAS, 423, 2270
Benkhoff J. et al., 2010, Planet. Space Sci., 58, 2
Bonanno C., Milani A., 2002, Celest. Mech. Dyn. Astron., 83, 17
Cicalò S., Milani A., 2012, MNRAS, 427, 468
Flamini E. et al., 2010, Planet. Space Sci., 58, 125
Huang C., Ries J. C., Tapley B. D., Watkins M. M., 1990, Celest. Mech., 48, 167
Iafolla V., Nozzoli S., 2001, Planet. Space Sci., 49, 1609
Iess L., Boscagli G., 2001, Planet. Space Sci., 49, 1597
Jehn R., Corral C., Giampieri G., 2004, Planet. Space Sci., 52, 727
Kaula W. M., 1966, Theory of Satellite Geodesy. Blaisdell, Waltham, MA
Kozai Y., 1965, AJ, 17, 395
Margot J. L. et al., 2012, J. Geophys. Res., 117, E00L09
Marra G., Colangeli L., Mazzotta Epifani E., Palumbo P., Flamini E., Debei S., 2005, in Pearsall T. P., Halls J., eds, Proc. SPIE Conf. Ser. Vol. 5962, Building European OLED Infrastructure. SPIE, Bellingham, 501
Mazarico E., Genova A., Goossens S., Lemoine F. G., 2014, J. Geophys. Res. Planets, 119, 2417
Milani A., Gronchi G. F., 2010, Theory of Orbit Determination. Cambridge Univ. Press, Cambridge
Milani A., Nobili A. M., Farinella P., 1987, Non-gravitational Perturbations and Satellite Geodesy. Adam Hilger, Bristol
Milani A., Rossi A., Vokroulicky D., Villani D., Bonanno C., 2001, Planet. Space Sci., 49, 1579
Milani A., Vokrouhlicky D., Villani D., Bonanno C., Rossi A., 2002, Phys. Rev. D, 66, 082001
Milani A., Tommei G., Vokrouhlicky D., Latorre E., Cicalò S., 2010, Proc. IAU Symp. 261, Relativity in Fundamental Astronomy: Dynamics, Reference Frames, and Data Analysis. Springer-Verlag, Berlin
Montenbruck O., Gill E., 2005, Satellite Orbits, Springer-Verlag, Berlin
Moyer T. D., 2000, Formulation for Observed and Computed Values of Deep Space Network Data Types for Navigation. Wiley, New York
Peale S. J., 1988, Rotational Dynamics of Mercury and the State of its Core. Univ. Arizona press, Tucson, AZ
Peale S. J., 2006, Icarus, 181, 338
Roy A. E., 2005, Orbital Motion, 4th edn. Taylor and Francis, London
Sánchez O. N., Belló M. M., Jehn R., 2006, Acta Astronaut., 58, 236
Schettino G., Cicalò S., Di Ruzza S., Tommei G., 2015, The relativity experiment of MORE: Global Full-cycle Simulation and Results IEEE, p. 141
Soffel M. et al., 2003, AJ,, 126, 2687
Solomon S. C., McNutt R. L., Jr, Gold R. E., Domingue D. L., 2007, Space Sci. Rev., 131, 3
Stark A. et al., 2015, Geophys. Res. Lett., 42, 7881
Tommei G., Milani A., Vokrouhlicky D., 2010, Celest. Mech. Dyn. Astron., 107, 285
Yseboodt M., Margot J. L., 2006, Icarus, 181, 327
Yseboodt M., Margot J. L., Peale S. J., 2010, Icarus, 207, 536
Yseboodt M., Rivoldini A., Van Hoolst T., Dumberry M., 2013, Icarus, 226, 41

This paper has been typeset from a TEX/LATEX file prepared by the author.